INTERNATIONAL JOURNAL FOR NUMERICAL METHODS IN FLUIDS
Int. J. Numer. Meth. Fluids 2005; **48**:801–818
Published online 11 March 2005 in Wiley InterScience (www.interscience.wiley.com). DOI: 10.1002/fld.940

CFD computations of NAL experimental airplane with rocket booster using overset unstructured grids

Fumiya Togashi[1,*,†,‡], Takeshi Fujita[1,‡], Yasushi Ito[1,‡], Kazuhiro Nakahashi[1,§] and Yoshikazu Makino[2,¶]

[1]*Department of Aerospace Engineering, Tohoku University, Aobaku Aramaki Aza Aoba 01, Sendai 980-8579-01, Japan*
[2]*National Aerospace Laboratory of Japan, Jindaiji Higashi-machi 7-44-1, Chofu-shi, Tokyo 182-8522, Japan*

SUMMARY

Flows around the NAL jet-powered experimental airplane with a small rocket booster under the fuselage are computed by solving the Euler equations using the overset unstructured grid method. The main objective of the present study is to evaluate the effect of a small rocket booster, which accelerates the airplane to supersonic speed, on the aerodynamic performance of the airplane during the ascent flight and the booster separation. Two unstructured meshes, one for the airplane and one for the booster, overlap. For the accurate separation simulation, the two bodies are in contact at first, and then the booster mesh is contact mesh is moved relative to the airplane mesh to evaluate flow interactions between two bodies. Copyright © 2005 John Wiley & Sons, Ltd.

KEY WORDS: CFD; overset method; unstructured mesh; separation; experimental airplane; NAL

1. INTRODUCTION

The National Aerospace Laboratory (NAL) of Japan is currently developing a small jet-powered experimental airplane as a part of the Next Generation Supersonic Transport project [1, 2]. One of the objectives of the project is to test the natural laminar wing designed by the CFD-based inverse design method. Following the unpowered airplane named NEXST1, the second model named NEXST2 has two jet engines under the wings for a cruising flight of Mach 1.6–2.

*Correspondence to: Fumiya Togashi, Department of Aerospace Engineering, Tohoku University, Aobaku Aramaki Aza Aoba 01, Sendai 980-8579-01, Japan.
† E-mail: togashi@ad.mech.tohoku.ac.jp
‡ Graduate student, Department of Aerospace Engineering.
§ Professor, Department of Aerospace Engineering.
¶ Research scientist.

Received 21 August 2003
Revised 4 November 2004
Accepted 15 December 2004

NEXST2 has a small rocket booster between the jet-engine nacelles in order to accelerate the airplane from transonic to supersonic speeds. The booster will be separated from the airplane at a Mach number of 1.8. The rocket booster is relatively small compared to the engine nacelles. However, when it is installed between the nacelles, the gap between the rocket and the nacelles is very small. Therefore, it is very important to evaluate the effect of the rocket booster on the overall aerodynamic characteristics of the airplane during the flight from transonic to supersonic, and when the booster is released from the airplane at supersonic speed. Shock waves are generated not only from the nose of the airplane but also from the nose of the booster and around the intakes of the nacelles. These shock waves interact with each other and produce a complex flowfield.

The objective of this study is to compute the flowfield of the NEXST2 during the ascent flight with the rocket booster and during the separation of the booster at supersonic speed.

To simulate the booster separation from the airplane by CFD, there are several approaches. The overset structured grid (Chimera) method is the most common approach for such a problem. This method was first introduced by Steger *et al.* [3] and Benek *et al.* [4] in 1980s. Currently this method is effectively used to solve both steady and unsteady Navier–Stokes computations for complex geometry [5–7] and for moving-body problems [8, 9]. Another approach is the deforming mesh method and has shown good results since 1980s [10, 11]. Recently the deforming mesh method becomes a powerful tool for treating moving-body problems [12–14].

In this paper, the overset unstructured grid method is used to compute flows around the NEXST2 airplane with the booster. The overset unstructured grid method has been proposed by the present authors and successfully applied to several problems [15–18]. The approach was also employed in References [19, 20]. Unstructured grids have great flexibility in handling complex geometries. By using unstructured grids for the overset concept, the number of submeshes required for covering the flowfield can be significantly reduced as compared with that needed in the overset structured grids. As a result, constructing interpolation stencils between grids becomes simple. Another advantage of this method is the capability for treatment of multiple bodies in contact [18]. Due to this capability, more precise simulation of separation becomes possible.

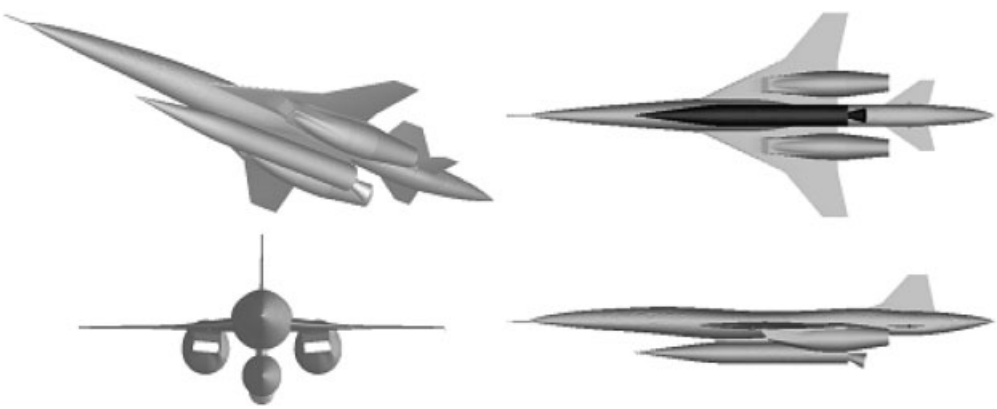

Figure 1. NAL jet-powered experimental airplane with a small rocket booster.

The NAL jet-powered experimental airplane has a relatively complicated configuration as shown in Figure 1. As mentioned above, the overset unstructured grid method is well suited to deal with multiple bodies in relative motion, especially when they have complicated configurations. It is also useful to evaluate the effect of the booster on the overall aerodynamic performance of the airplane in ascent flight. With the overset approach, adding/deleting the booster or changing the relative position of the booster to the airplane can be easily conducted without generating new meshes.

In this paper, computational methods to treat complex geometry of the airplane with a small booster and to handle the moving body for the separation process are discussed and then effects of the small booster on the flowfield of the airplane during the ascent flight and the separation process are discussed in detail.

2. OVERSET PROCEDURE

There are two major steps to establish intergrid communications in the overset method:

1. Hole cutting, which involves dividing all points of each subgrid into two groups, active and non-active points.
2. Identification of interpolation stencils, which involves a search of donor cells for all intergrid-boundary points.

The second step, identification of interpolation stencils, is straightforward for unstructured grids. Once a donor cell is identified, values on the point in this cell are interpolated from values on the vertex of the cell using the area co-ordinates for a triangle and the volume co-ordinates for a tetrahedral cell. In the present approach, the donor cell for the interpolation at each intergrid-boundary point is identified during the process of hole cutting. Therefore, the first step is discussed here.

The identification of the intergrid boundary for multiple body problems must be performed completely automatically to fully take advantage of the overset unstructured grid approach. The efficiency and robustness of the hole-cutting procedure is particularly important for moving-body problems. Here the wall distance is used as a basic parameter to construct the intergrid boundary. Nodal points which are closer to the wall boundary of their own grid are defined as a computational field [15, 16].

Let us consider an example of the hole-cutting procedure. In Figure 2, suppose that the broken lines show the grid (Grid-A) generated around Body-A, and the solid lines show that (Grid-B) for Body-B. Node i belongs to Grid-A, and then, the donor cell in Grid-B is indicated by a-b-c in Figure 2. The minimum wall distance of this node i to Body-A is compared with the wall distance of the donor cell to Body-B. The distance of the donor cell is evaluated by a linear interpolation from its vertex values. Since the wall distance of the node i to Body-A is shorter than that of donor cell a-b-c to Body-B, Node i is assigned as an active node (belongs to computational field). In contrast, node j in Figure 2 is selected as a non-active node. In this way, all nodal points in the overlapping region are assigned as active (computational) or non-active (non-computational) nodes.

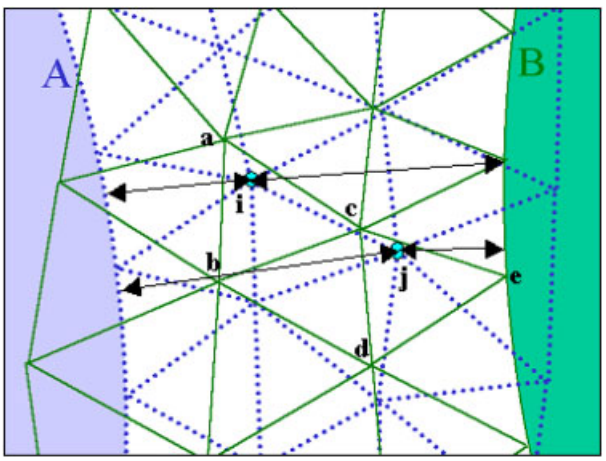

Figure 2. Determination of intergrid boundary between grid A(···) and grid B(−).

3. DONOR CELL SEARCHING

To construct the intergrid boundary, all nodal points must find their donor cells among the overset grids. The required number of searching process can easily become more than one million for three-dimensional problems. Therefore, an efficient and reliable search algorithm is necessary.

In this study, Lawson's neighbour-to-neighbour jump search algorithm [21] is utilized. The method is based on jump to the neighbouring cell that locates to the target side of the current cell as schematically shown in Figure 3(1). For example, the current cell is the triangle a-b-c in Figure 3(1). For each edge of the triangle a-b-c, on which side the target is located is examined. Concerning the edge b-c of the triangle a-b-c, the nodal points a, d, f and h are located inner side and the nodal points e, g and i are located outer side. In Figure 3(1), the target is located on the inner side of the current cell relative to the edges a-b and a-c, however, the target is located on the outer side of the current cell relative to the edge b-c. So, the next cell is the triangle b-e-c. In the triangle b-e-c, the target is located on the outer side relative to the edge c-e only and it is located on the inner side of the cell relative to the edges b-c and b-e. The following cell becomes the triangle c-e-g. By repeating this procedure, the succeeding cells become the triangles c-e-g, c-g-h, and h-g-i, which is the cell including the target point. To judge if the target point is located inside the current cell or not, the volume of the tetrahedron composed of the target point and the three vertexes of the current cell is calculated as shown in Figure 3(2). If all the volumes (four tetrahedrons are composed of the target and each face of the current cell are calculated) are positive, the target point is located inside the current cell. Flow variables are also averaged by these volumes. The variables are averaged by using the ratio of each volume that is composed of the recipient point and each face of the current cell to the total volume of the current cell.

This searching process is very efficient because the search path becomes one-dimensional even in the three-dimensional field. However, the result highly depends on the starting point. As shown in Figure 4(a), the search starting from point A succeeds in reaching the target.

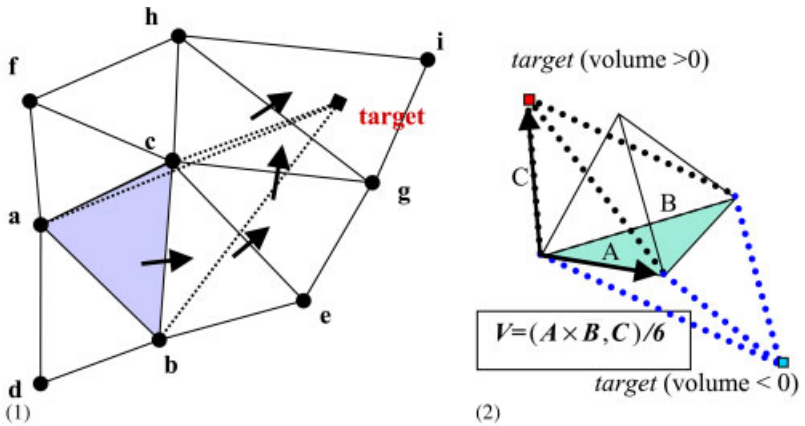

Figure 3. (1) Selection of the next cell among three neighbours; and (2) donor cell searching.

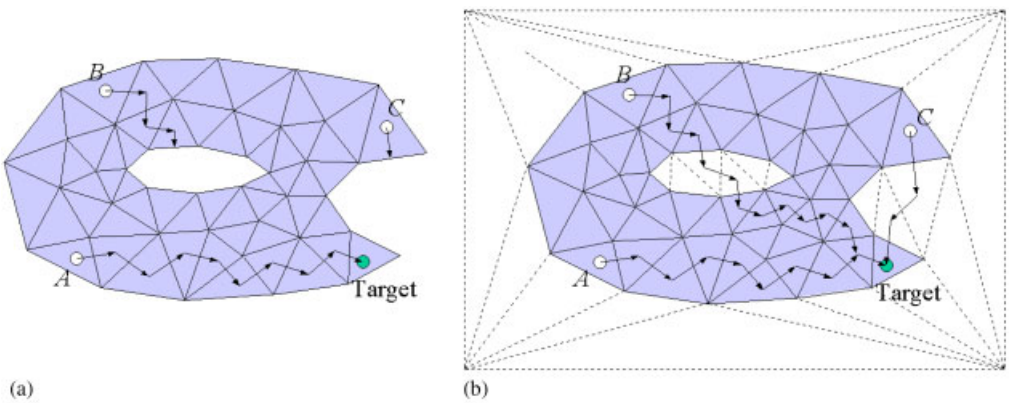

Figure 4. Neighbour-to-neighbour search: (a) searches from B and C fail; and (b) searches in a convex domain.

However, searching from B and C get stuck at the body boundary or the outer boundary. For these cases, the search has to be restarted by changing the starting cells.

To avoid this uncertainty of the searching process, the search domain is modified to become a convex hexahedron in three dimensions for any computational geometry. This is done by adding subsidiary meshes into the bodies and outside of the computational region as shown in Figure 4(b). Because the Delaunay triangulation [22] is employed for the mesh generation, the subsidiary meshes can be obtained automatically as a byproduct of the mesh generation procedure. By utilizing the subsidiary meshes, the Lawson's method becomes more reliable and efficient.

For multiple moving-body problems, the intergrid-boundary definition must be as efficient as possible. Since the efficiency of the donor cell search depends on the initial guess, the

computational work for the second search after the initial hole cutting is reduced significantly. Moreover, once the initial hole cutting is performed, the search of the donor cells after a small relative movement of the subgrid can be limited to cells around the previous donor cell.

4. FLOW SOLVER

In the present method, the computational domain consists of several unstructured subgrids, which may overlay each other. The unstructured subgrids generated around each component in the flowfield are put together to discretize the whole computational domain. The Euler equations are solved in each subgrid with the proper boundary conditions.

The Euler equations for compressible inviscid flows are written in an integral form as follows:

$$\frac{\partial}{\partial t}\int_{\Omega}\mathbf{Q}\,\mathrm{d}V+\int_{\partial\Omega}\mathbf{F}(\mathbf{Q})\cdot\mathbf{n}\,\mathrm{d}S=0 \tag{1}$$

where $\mathbf{Q}=[\rho,\rho\boldsymbol{u},\rho\boldsymbol{v},\rho\boldsymbol{w},\boldsymbol{e}]^{\mathrm{T}}$ is the vector of conservative variables; ρ the density; u, v and w the velocity components in the x, y and z directions; and e is the total energy. The vector $\mathbf{F}(\mathbf{Q})$ represents the inviscid flux vector and $\mathbf{n}$ is the outward normal of $\partial\Omega$, which is the boundary of the control volume Ω. This system of equations is closed by the perfect gas equation of state.

The equations are solved by a finite volume cell-vertex scheme. The control volume is a non-overlapping dual cell. For the control volume, Equation (1) can be written in an algebraic form as follows:

$$\frac{\partial\mathbf{Q}_i}{\partial\boldsymbol{t}}=-\frac{1}{\boldsymbol{V}_i}\sum_{j(i)}\Delta\boldsymbol{S}_{ij}\mathbf{h}(\mathbf{Q}_{ij}^{+},\mathbf{Q}_{ij}^{-},\mathbf{n}_{ij}) \tag{2}$$

where $\Delta\boldsymbol{S}_{ij}$ is the segment area of the control volume boundary associated with the edge connecting points i and j. This segment area, $\Delta\boldsymbol{S}_{ij}$, as well as its unit normal, $\mathbf{n}_{ij}$, can be computed by summing up the contribution from each tetrahedron sharing the edge. The term $\mathbf{h}$ is an inviscid numerical flux vector normal to the control volume boundary, and $\mathbf{Q}_{ij}^{\pm}$ are the values on both sides of the control volume boundary. The subscript of summation, $j(i)$, represents all nodal points connected to node i.

The numerical flux, $\mathbf{h}$, is computed using the approximate Riemann solver of Harten-Lax-van Leer-Einfeldt-Wada [23]. Second order spatial accuracy is realized by a linear reconstruction of the primitive gas dynamic variables with Venkatakrishnan's limiter [24].

The LU-SGS implicit method [25] is applied to integrate Equation (2) in time. With $\Delta\mathbf{Q}=\mathbf{Q}^{n+1}-\mathbf{Q}^{n}$ and a linearization of the numerical flux term as $\mathbf{h}_{ij}^{n+1}=\mathbf{h}_{ij}^{n}+\mathbf{A}_i^{+}\Delta\mathbf{Q}_i+\mathbf{A}_j^{-}\Delta\mathbf{Q}_j$, the final form of the LU-SGS method on an unstructured grid becomes:

Forward sweep:

$$\Delta\mathbf{Q}_i^{*}=\mathbf{D}^{-1}\left[\mathbf{R}_i-0.5\sum_{j\in L(i)}\Delta\boldsymbol{S}_{ij}(\Delta\mathbf{h}_j^{*}-\rho_A\Delta\mathbf{Q}_j^{*})\right] \tag{3a}$$

Backward sweep:

$$\Delta\mathbf{Q}_i = \Delta\mathbf{Q}_i^* - 0.5\mathbf{D}^{-1} \sum_{j\in U(i)} \Delta\boldsymbol{S}_{ij}(\Delta\mathbf{h}_j - \rho_A \Delta\mathbf{Q}_j) \tag{3b}$$

where $\mathbf{R}_i = -\sum_{j(i)} \Delta\boldsymbol{S}_{ij}\mathbf{h}_{ij}^n$, $\Delta\mathbf{h} = \mathbf{h}(\mathbf{Q}+\Delta\mathbf{Q}) - \mathbf{h}(\mathbf{Q})$ and $\mathbf{D}$ is a diagonal matrix derived by the Jameson–Turkel approximation of Jacobian [26] as $\mathbf{A}^{\pm} = 0.5(\mathbf{A} \pm \rho_A\mathbf{I})$, where ρ_A is the spectral radius of Jacobian $\mathbf{A}$. $\mathbf{D}$ is given as follows:

$$\mathbf{D} = \left(\frac{\boldsymbol{V}_j}{\Delta\boldsymbol{t}} + 0.5\sum_{j(i)} \Delta\boldsymbol{S}_{ij}\rho_A\right)\mathbf{I} \tag{4}$$

The lower/upper splitting of Equation (3), namely $j \in L(i)$ and $j \in U(i)$, for the unstructured grid is realized by using a grid reordering technique [25] to improve the convergence and the vectorization.

5. OVERSET IMPLEMENTATION

In addition to the boundaries of the computational domain, subgrids may have holes and intergrid boundaries with the neighbouring donor-subgrids. The nodal points belonging to the non-computational field must be blanked out from the flowfield solution. To classify whether the nodal points should be computed or not in the flow solver, all nodal points have information as to whether they belong to the computational field or not. Namely,

$$\text{IBLANK} = \begin{cases} 1, & \text{a point is not blanked out node.} \\ 0, & \text{a point is blanked out node.} \end{cases}$$

This value is 1 or 0 depending on the area inside or outside the computational subregion. In the flow solver, the conservative variables and the gradient variables are multiplied by the value IBLANK(i); namely, the variables in the outside region (hole region) are temporarily set to zero. Each grid is first computed and then flow variables are interpolated around intergrid boundary. If the node whose IBLANK is 0 has a partner cell which belongs to the computational field, the node is interpolated from the flow variables from the partner cell. That is, the node of IBLANK = 0 is never computed. Although it has the variables given by its partner grid. Due to this procedure, computational accuracy around the intergrid boundary is highly improved.

6. TREATMENT OF MULTIPLE BODIES IN CONTACT

A similar procedure can be applied to multiple bodies in contact. The procedure is shown in Figure 5 and can be explained as follows. In Figure 5, nodal point A (circular-shaped) belongs to Body 1 (light grey zone), nodal points a, b and c and the other square-shaped and diamond-shaped points belong to the Body 2 (dark grey zone). Solid lines show the mesh

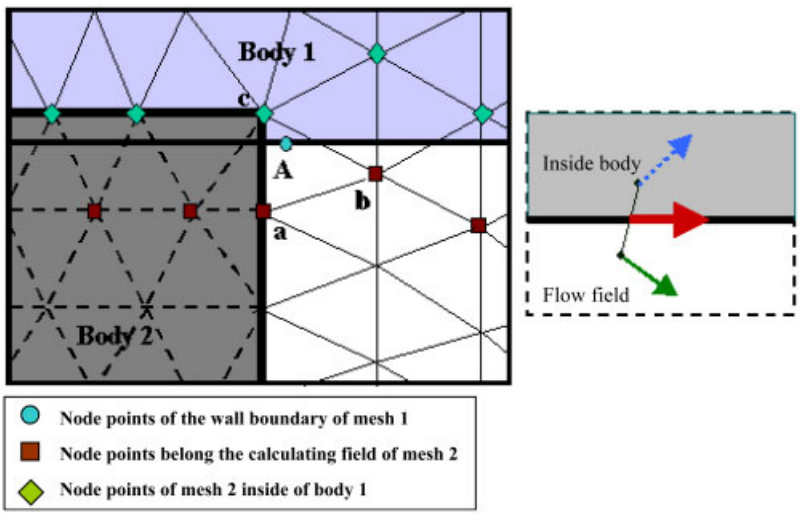

Figure 5. Treatment of multiple bodies in contact.

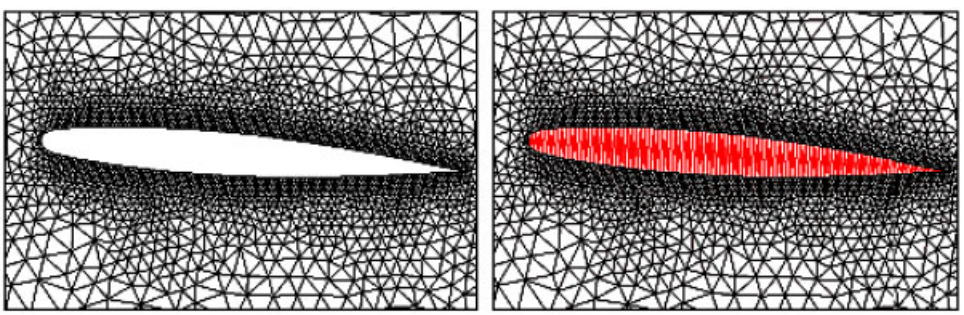

Figure 6. Inner mesh which is the mesh generated inside the body.

generated around Body 2 and dotted lines show the mesh of the wall boundary of Body 2:

1. First of all, every nodal points located inside computational field are computed. Then, the nodal points located outside the partner body and whose IBLANK set to 0 (e.g. nodal point b) are interpolated from their donor cells.
2. Nodal points which are located inside another body (e.g. diamond-shaped nodal points are located inside Body 1), have their IBLANK set to 0.
3. Checking all edges, if one nodal point is located in the flowfield (e.g. square-shaped nodal points) and the other is located inside a body (e.g. diamond-shaped nodal points), the wall boundary condition is applied to the edge. The nodal point that is located inside the body is given the density and pressure of the opposite nodal point, while the velocity is defined to realize the slip condition between the two nodal points (namely, the normal

vector of the wall boundary is used and the velocity of the edge realize the slip condition bestriding the wall boundary). Due to applying this procedure to all edges, the nodal point inside body has averaged values from the connected nodal points and the accuracy around the intersection region is increased.

4. If the nodal points that are inside a grid body do not have a neighbouring nodal point in the flowfield, the nodes are interpolated the flow variables from the inner mesh which is generated inside the body (Figure 6).
5. Due to the above treatment, nodal point c has some non-zero flow variables and nodal point A obtains adequate flow variables from the interpolation of the partner-cell a-b-c.

The procedure mentioned above is important a separating simulation. Originally, the inner mesh is generated for fast and accurate search for the partner cell and thus the search can pass through the inside of the body. However, the inner mesh is a very important factor for problems of separation. The nodal points which are inside the body (namely, the partner cell belongs to the inner mesh) have proper variables so they can be computed even when they enter the computational field during the separation.

7. COMPUTATIONAL RESULTS

7.1. Unstructured meshes

Figure 7 shows a tetrahedral unstructured grid generated around the jet-powered experimental airplane [27–29]. Flow-through nacelles are assumed as was employed by a wind tunnel model. The airplane has a relatively complicated configuration due to the nacelles. However, owing to the unstructured mesh, the full configuration can be described by only one unstructured grid. The numbers of nodes and cells are 744 142 and 4 091 850, respectively. The number of surface nodes is 224 768 that are appropriately distributed as shown in Figure 7 so as to resolve the sharp leading edges and corners.

For flow simulations around a configuration of the airplane with a small booster rocket under the fuselage, an unstructured mesh that covers a cylindrical region around the booster is overlapped with the airplane mesh as shown in Figure 8(A). The number of nodes of the

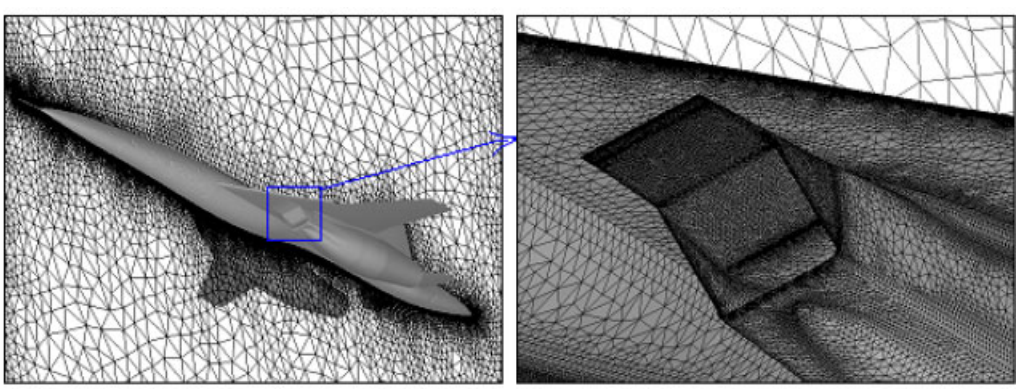

Figure 7. Unstructured mesh generated around the experimental airplane.

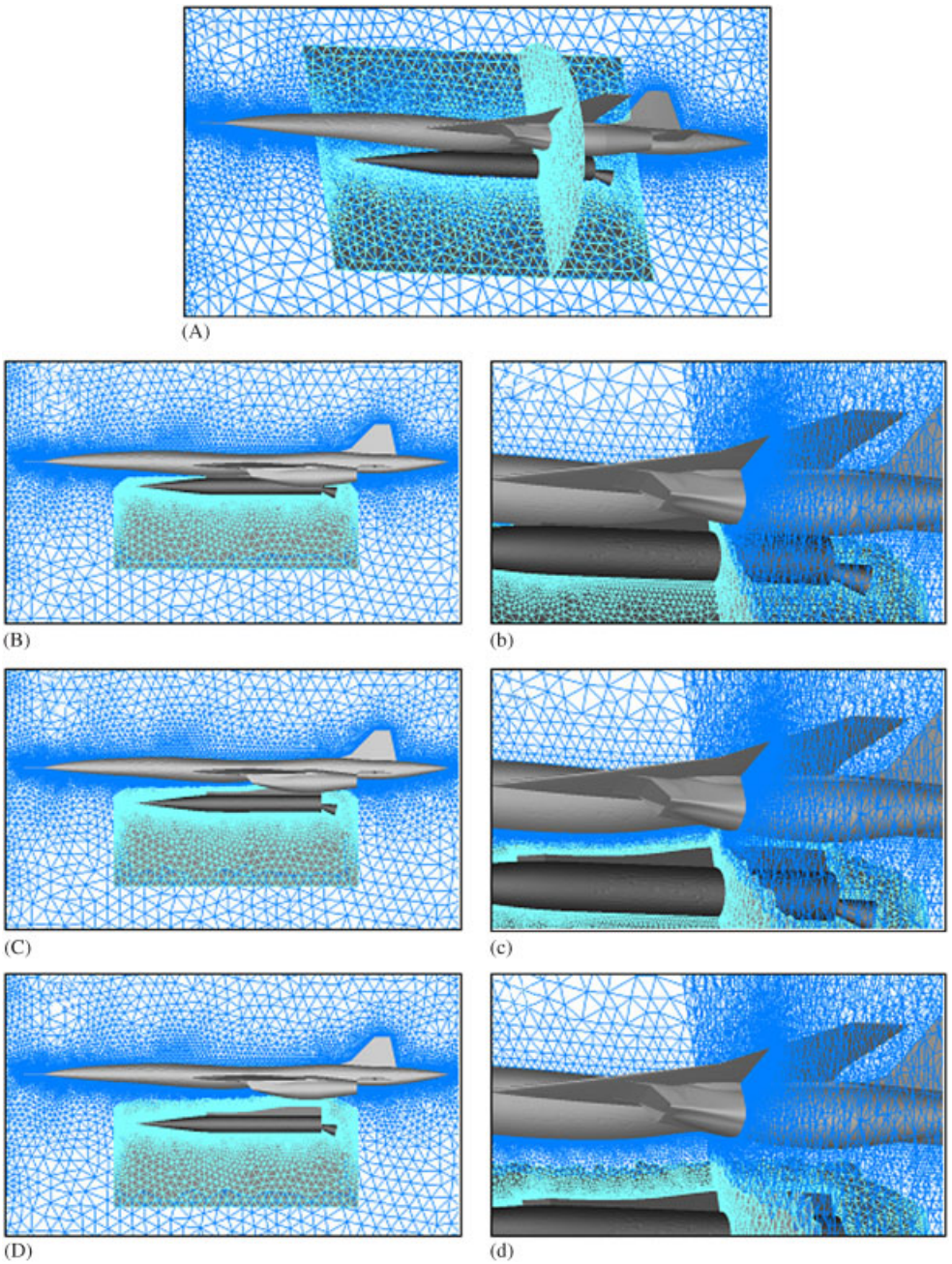

Figure 8. Overset grids: (A) before the intergrid definition; and (B–D) after the intergrid definition.

booster mesh is 63 139. Connecting parts between the airplane and the rocket booster are embedded in the lower surface of the experimental airplane. Figure 8(B)–(D) show cut views of the two grids after the overset implementation during the separation. Figure 8(b)–(d) show enlarged views, respectively.

7.2. Flow simulation of airplane with booster

Flow computations around the airplane with a booster rocket under the fuselage are conducted for several freestream Mach numbers and angles of attack. The boundary condition of the rocket exhaust is defined as the wall boundary for the comparison with the wind tunnel data.

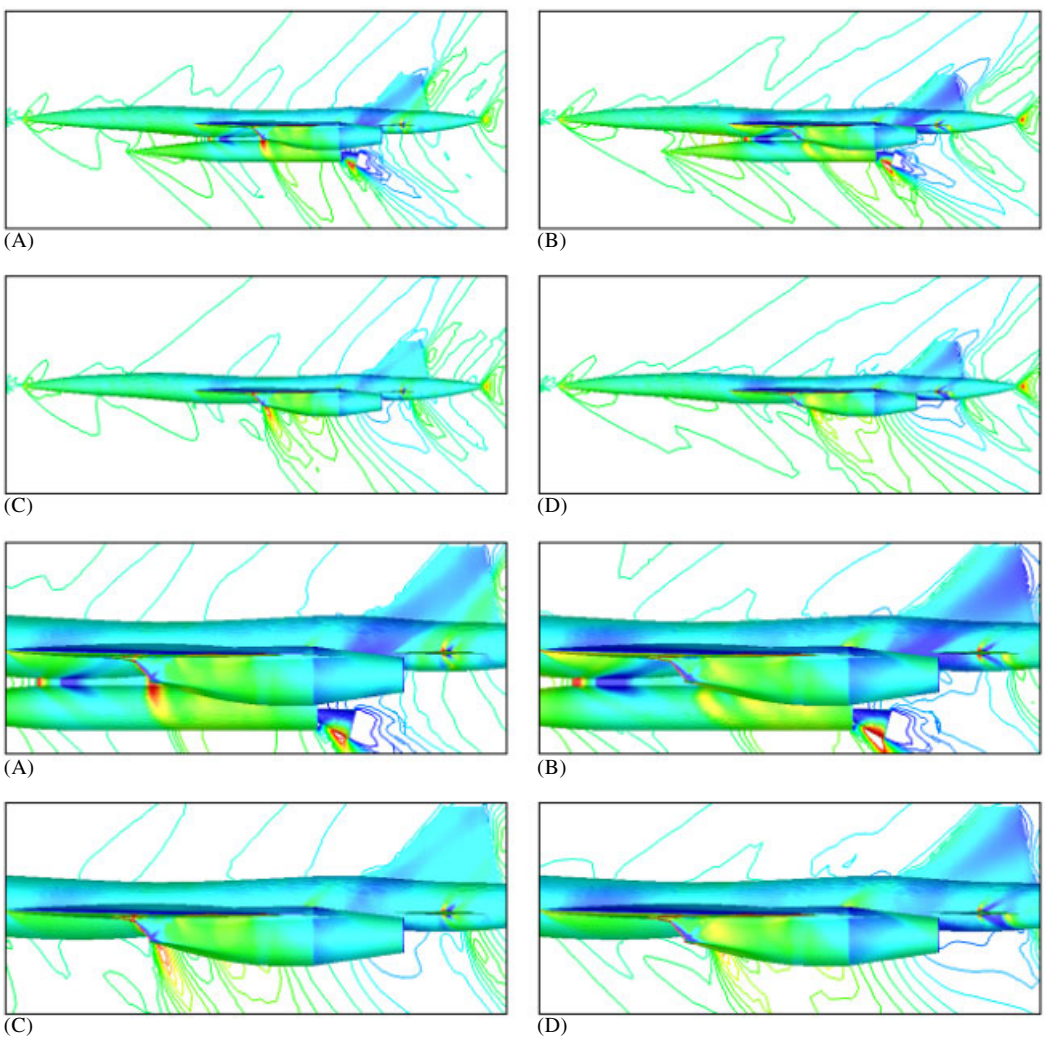

Figure 9. Computed pressure contours of the airplane and booster and enlarged views around the intake with and without a small booster: (A) and (C) $M_\infty = 1.4$, $\alpha = 5.0$; and (B) and (D) $M_\infty = 1.7$, $\alpha = 4.9$.

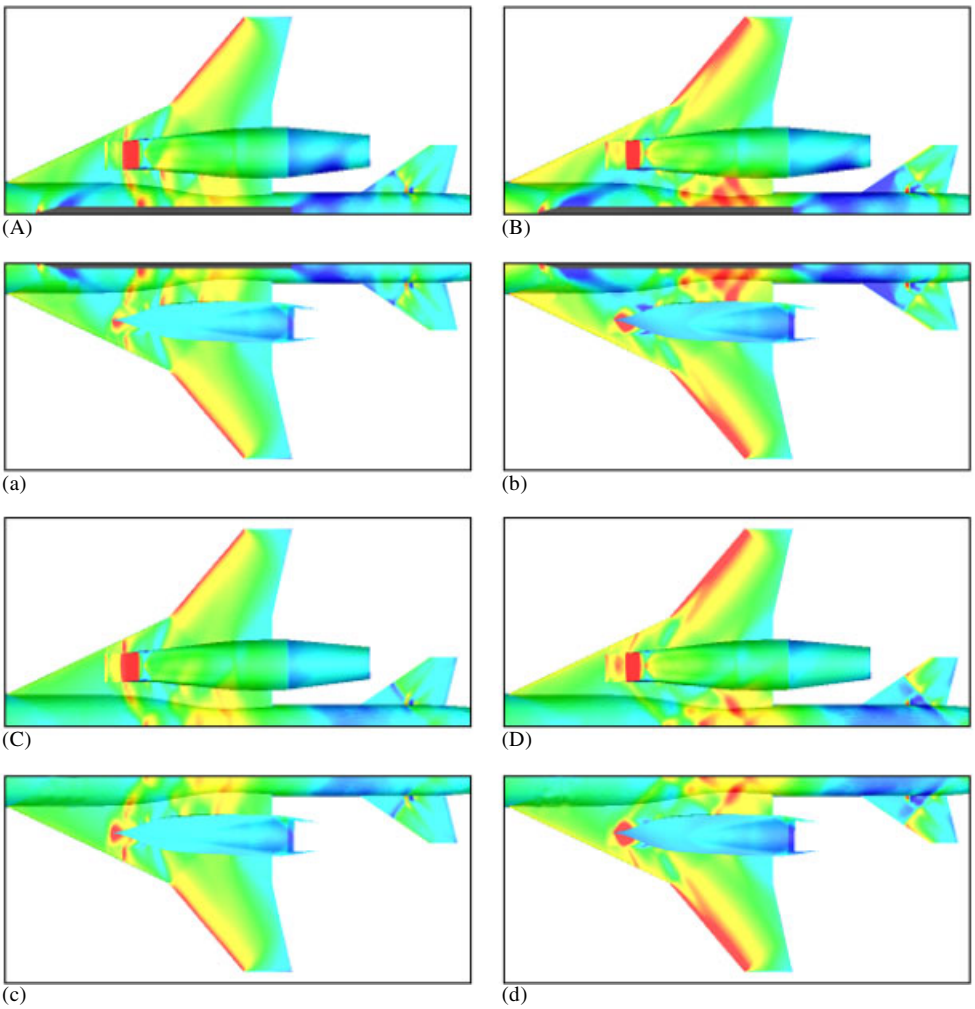

Figure 10. Computed pressure contours on the lower surface of the airplane: (A) and (C) $M_\infty = 1.4$, $\alpha = 5.0$; (B) and (D) $M_\infty = 1.7$, $\alpha = 4.9$; and (a), (b), (c) and (d) computed pressure contours of the lower surface of the airplane not describing the nacelle.

Figure 9 shows the computed pressure contours on the surface and the symmetrical plane for freestream Mach numbers of 1.4 and 1.7 with angle of attack of about 5° of unsteady flow computation. Figure 10 shows the computed pressure contours on the lower surface of the airplane where in Figure 10(a)–(d) the nacelle of the airplane is not depicted.

A shock generated from the nose of the booster affects on the lower surface of the airplane. Shocks are also generated from the front of the connecting parts between the airplane and booster, lower surface of the booster nozzle and the diverter of the airplane. Especially, the shock waves from the tip and the side of the diverter of the airplane relatively strongly affects on the lower surface of the airplane fuselage and complexly reflected among the nacelle, the

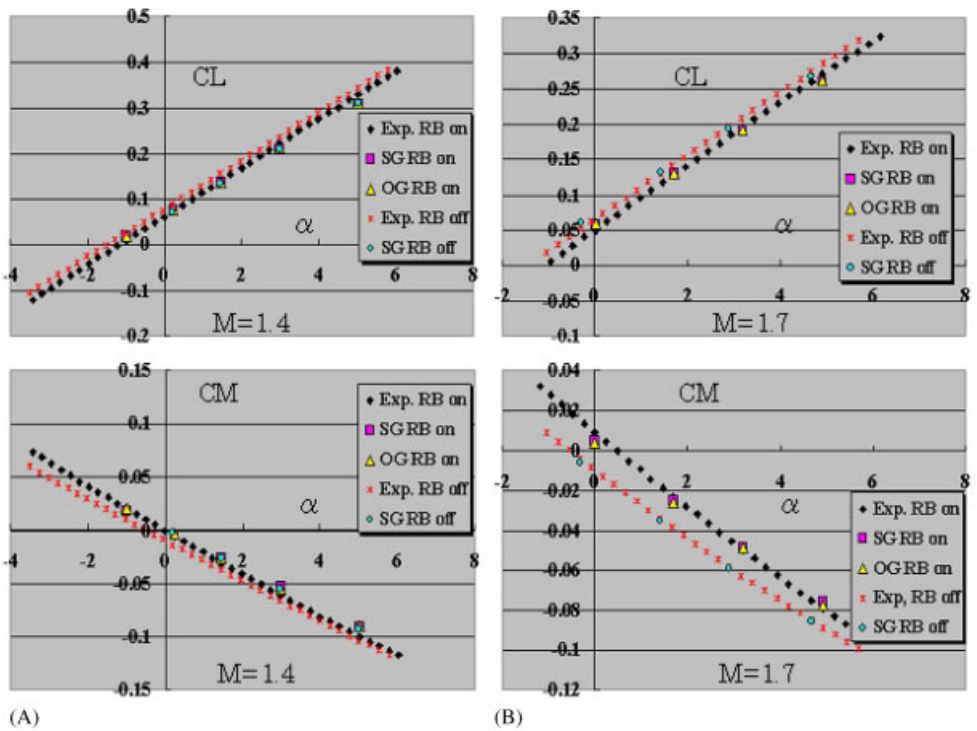

Figure 11. Comparisons of the lift and pitching moment coefficients between the experimental and computational results: (A) at $M_\infty = 1.4$; and (B) at $M_\infty = 1.7$.

lower surface of the airplane and the upper surface of the booster (Figures 9(A), (B), 10(A) and (B)). The expansion waves are also observed from the corner of the connecting parts and the tail of the booster. The expansion wave generated from the corner of the connecting parts affects on the intake of the nacelle at a Mach number of 1.4 and in case of a Mach number of 1.7, it affects on the sidewall of the nacelle. The expansion wave generated from the tail of the booster affects on the lower surface of the tail of the airplane fuselage and on the rear part of the nacelle at Mach 1.4 (Figure 10(A)). It also affects on the tail wing of the airplane at Mach 1.7 (Figure 10(B)). The affect of the booster is relatively larger around the tail of the airplane (Figures 9 and 10). At high Mach number like a Mach number of 1.7, the attachment of the booster affects on the tail wing of the airplane (Figure 10(B)). A relatively higher-pressure zone around the centre of the connecting parts is also observed by the attachment of the booster in Figure 10.

Figure 10 shows comparisons of the computed lift and pitching moment coefficients with the wind tunnel tests by NAL. To confirm the validity of the overset mesh method, computed results using an unstructured single grid is also plotted in the figures. In Figure 11, 'RB on' and 'RB off' denotes the computational results of the airplane with a small rocket booster case and the airplane without a booster case, respectively. 'SG' denotes the computational results of a single grid case and 'OG' denotes the computational results of overset unstructured grid

case. The computational results show good agreement between the overset grid case and the single grid case.

The effect of the booster on the overall lift coefficients is relatively small. However, the pitching moment coefficients are affected by the attachment of the booster, especially for higher Mach number with small angle of attack.

7.3. Flow simulation of booster separation

Flowfield during the separation of the rocket booster from the airplane is simulated using the overset unstructured grid method under the assumption of the unsteady flow. At first, the rocket booster is in contact with the airplane, and then the booster begins the separation. The movement is subject to the gravity and the other force is not considered.

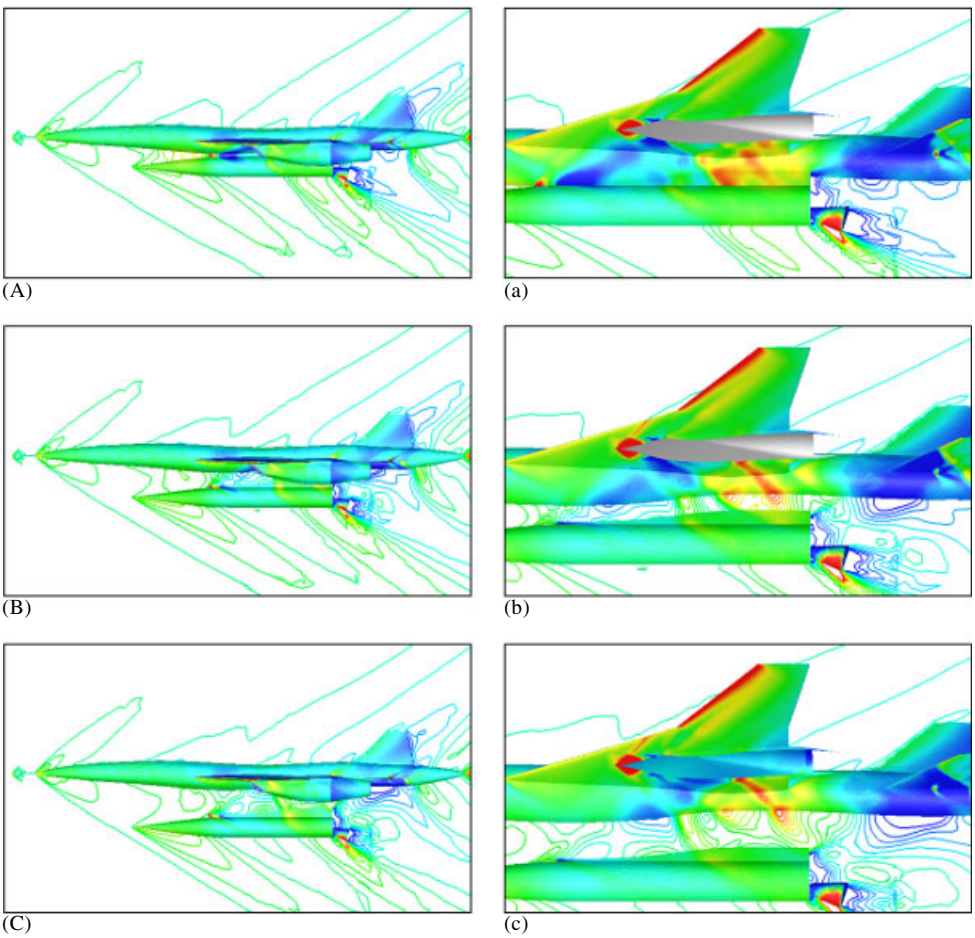

Figure 12. Computational results of separation: Pressure contours of the airplane-rocket booster at freestream $M_\infty = 1.8$ and $\alpha = 3.0^\circ$ (airplane): (A) and (a) $D = 0.0$; (B) and (b) $D = 0.025$; (C) and (c) $D = 0.05$.

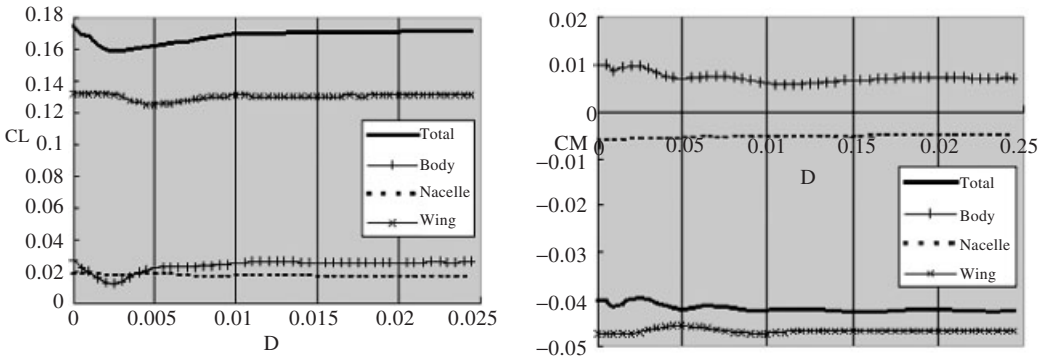

Figure 13. Lift and pitching moment coefficients of the airplane during the separation.

Figure 12 shows the pressure distributions during the separation. Figure 12(a)–(c) also show the pressure distributions on the surface of the airplane and symmetric plane (The structure of the grids and the boundaries of the overlapping grids are shown in Figure 8). The nacelle is not depicted in these pictures in order to show the pressure distribution on the fuselage.

A shock wave generated from the diverter is reflected on the fuselage of the airplane at first. Then the reflected shock is reflected again on the upper surface of the booster. Finally, the complexly reflected shock wave is impinged on the lower surface of the airplane (Figure 12(a)–(c)).

Figure 13 shows the lift and pitching moment coefficients of the airplane during the separation. The value D denotes the distance between the airplane and booster. This value is normalized by the total length of the airplane (12 m). The lift coefficients are slightly decreased because the high-pressure zone in front of the connecting parts is disappeared due to the separation of the booster. Then the lift coefficients are increased gradually. The pitching moment coefficients show temporary decreases just at the beginning of the separation and then show slight vibration.

Figure 14 shows the pressure distribution on the symmetric surface of the airplane. Figure 14(A) shows the pressure distribution before the separation. Due to the existence of the connecting parts, the pressure coefficient on the lower surface from $x/L = 0.43$ to $x/L = 0.7$ is 0. In Figure 14(B), at the beginning of the separation, the expansion wave generated from the corner of the connecting part impinges the lower surface of the airplane around $x/L = 0.48$. This impinged point of the expansion wave moves downward along with the booster separation in Figure 14(C) and (D). The shock wave generated from the diverter causes the peak value around $x/L = 0.6$ in Figure 14(B)–(D). Another expansion wave is generated from the tail of the small booster. This expansion wave impinges on the lower surface of the airplane fuselage around $x/L = 0.76$ in Figure 14(B). The area of the lower surface where the expansion wave impinges also moves downward during the separation and affects on the tail wing of the airplane in Figure 14(C) and (D).

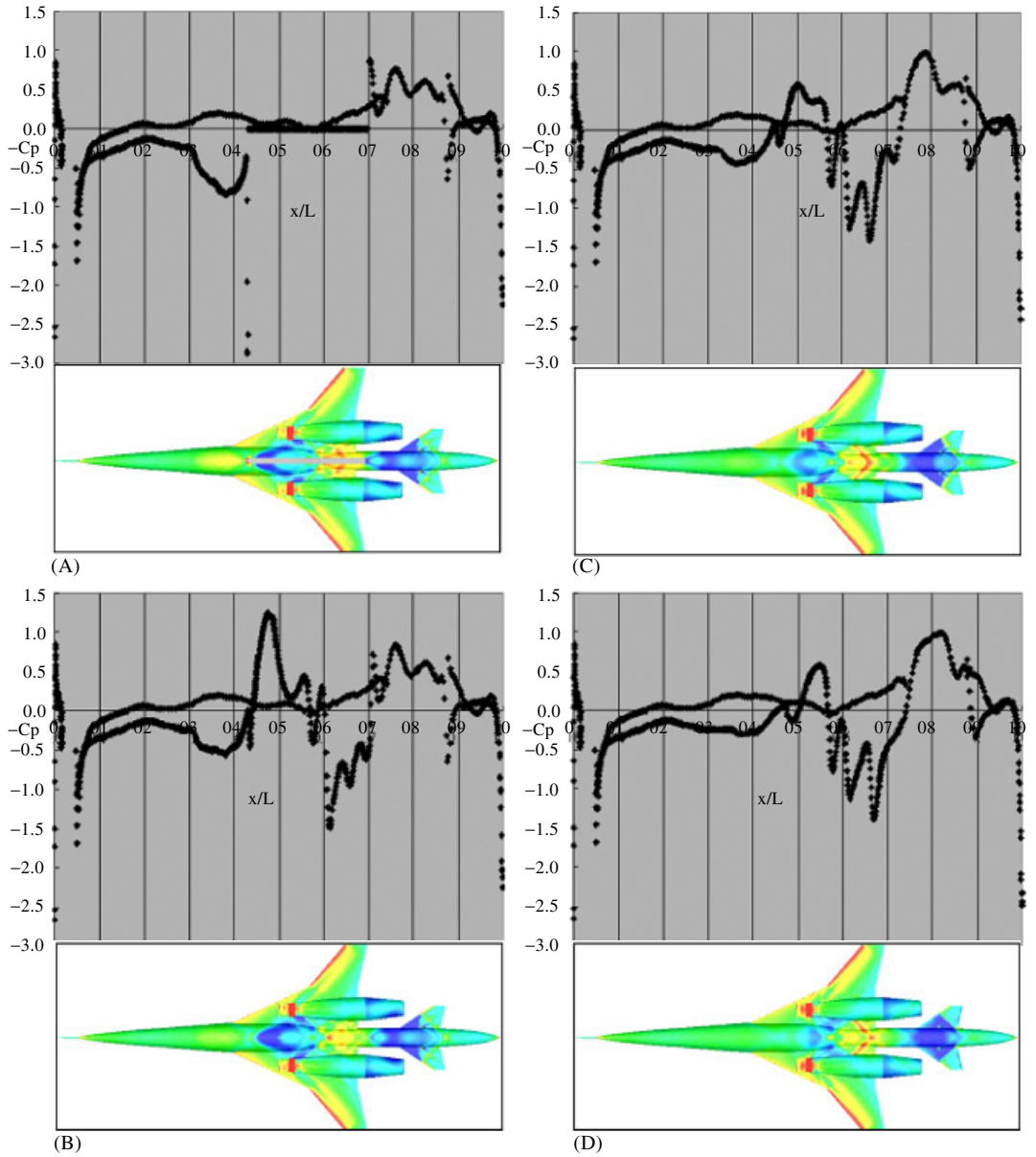

Figure 14. Pressure distributions on the symmetric boundary of the airplane and pressure distributions on the lower surface of the airplane: (A) $D = 0$; (B) $D = 0.005$; (C) $D = 0.025$; and (D) $D = 0.05$.

8. CONCLUSION

The overset unstructured grid method was applied to an NAL jet-powered experimental airplane with a small rocket booster. The computed results for a full configuration at ascent flight

condition depicted the complex shock reflection patterns occurred under the airplane under-surface. The accuracy of the overset unstructured grid method was confirmed by comparing with experimental results and the result by unstructured grid case.

The method was then applied to simulate the booster separation from the NAL experimental airplane. The computational results revealed the complex shock wave patterns between the two bodies during the separation. These shock waves are generated not only from the nose of the booster but also from the diverter of the airplane and the connecting part of the booster and complexly affect on each other. The expansion waves generated from the booster also affects on the lower surface of the airplane.

The overset unstructured grid method was shown its capability to treat flow problems around complex multiple bodies with relative motions. The method is also applied to successive computations with changing the location of the booster without regenerating new meshes of the airplane and the booster. Such computations are very useful to evaluate the best position of the booster for launch configuration and the separation.

REFERENCES

1. Iwamiya T. NAL SST project and aerodynamic design of experimental aircraft. *Proceedings of the 4th ECCOMAS Computational Fluid Dynamics Conference*, Athens. Wiley: Chichester, U.K., 1998; 580–585.
2. Yoshida K, Noguchi M, Shimbo Y, Kuroda F. Comparison of wind tunnel test and CFD analysis on an airframe/nacelle configuration of the scaled supersonic experimental airplane. *Proceedings of the 39th Aircraft Symposium*, Gifu, Japan, 2001 (in Japanese).
3. Steger JL, Dougherty FC, Benek JA. A chimera grid scheme. *ASME Mini-Symposium on Advances in Grid Generation*, 1982.
4. Benek JA, Buning PG, Steger JL. A 3-D chimera grid embedding technique. *AIAA 85-1523*, 1985.
5. Merkin RL. On adaptive refinement and overset structured grids. *AIAA 97-1858*, 1997.
6. Cao HV, Su TY. Navier–Stokes analyses of a 747 high lift configuration. *AIAA Paper 98-2623*, 1998.
7. Rogers SE, Cao HV, Su TY. Grid generation for complex high-lift configurations. *AIAA Paper 98-3011*, 1998.
8. Nichols RH, Tramel RW. Applications of a highly efficient numerical method for overset-mesh moving body problems. *AIAA Paper 97-2255*, 1997.
9. Lee Y, Baeder JD. High-order overset method for blade vortex interaction. *AIAA Paper 2002-0559*, 2002.
10. Batina JT. Unsteady Euler airfoil solutions using unstructured dynamic meshes. *AIAA Paper 89-0115*, 1989.
11. Lohner R, Baum JD. Three-dimensional store separation using a finite element solver and adaptive remeshing. *AIAA 91-0602*, 1991.
12. Murayama M, Nakahashi K, Matsushima K. Unstructured dynamic mesh for large movement and deformation. *AIAA Paper 2002-0122*, 2002.
13. Murayama M, Togashi F, Nakahashi K, Matsushima K, Kato T. Simulation of aircraft response to control surface deflection using unstructured dynamic grids. *AIAA 2002-2940*, 2002.
14. Hassan O, Sorensen KA, Weatherill NP, Morgan K. Mesh adaptation for time-accurate inviscid and viscous compressible fluid flow. *8th Numerical Grid Generation in Computational Field Simulations*, Honolulu, Hawaii.
15. Nakahashi K, Togashi F, Sharov D. Intergrid-boundary definition method for overset unstructured grid approach. *AIAA Journal* **38**(11):2077–2084.
16. Togashi F, Nakahashi K, Ito Y, Shinbo Y, Iwamiya T. Flow simulation of NAL experimental supersonic airplane/booster separation using overset unstructured grids. *Computers and Fluids* 2001; **30**:673–688.
17. Togashi F, Ito Y, Murayama M, Nakahashi K, Kato T. Flow simulation of flapping wings of an insect using overset unstructured grid. *AIAA-2001-2619*, 2001.
18. Togashi F, Ito Y, Nakahashi K, Obayashi S. Extensions of overset unstructured grids to multiple bodies in contact. *AIAA-2002-2809*, 2002.
19. Lohner R, Sharov D, Luo H, Ramamurti R. Overlapping unstructured grids. *AIAA-2001-0439*, 2001.
20. Luo H, Sharov D, Baum JD. An overlapping unstructured grid method for viscous flows. *AIAA-2001-2603*.
21. Takeo Taniguchi. *Automatic Element Division for FEM*. Morikita Publishing House, 1992 (in Japanese).
22. Bowyer A. Computing dirichlet tessellations. *The Computer Journal* 1981; **23**(2):162–166.
23. Obayashi S, Guruswamy GP. Convergence acceleration of an aeroelastic Navier–Stokes solver. *AIAA Paper 94-2268*, 1994.
24. Venkatakrishnan V. On the accuracy of limiters and convergence to steady state solutions. *AIAA Paper 93-0880*, 1993.

25. Sharov D, Nakahashi K. Reordering of hybrid unstructured grids for lower–upper symmetric Gauss–Seidel computations. *AIAA Journal* 1998; **36**(3):484–486.
26. Jameson A, Turkel E. Implicit schemes and LU decompositions. *Mathematics of Computation* 1981; **37**(156):385–397.
27. Ito Y, Nakahashi K. Direct surface triangulation using stereolithography data. *AIAA Journal* 2002; **40**(3): 490–496.
28. Ito Y, Nakahashi K. Surface triangulation for polygonal models based on CAD data. *International Journal for Numerical Methods in Fluids* 2002; **39**(1):75–96.
29. Sharov D, Nakahashi K. A boundary recovery algorithm for Delaunay tetrahedral meshing. *Proceedings of the 5th International Conference on Numerical Grid Generation in Computational Field Simulations*, 1996; 229–238.

